Modeling and Stability Analysis of Active/Hybrid Common-Mode EMI Filters for DC/DC Power Converters

Yongbin Chu, *Student Member, IEEE*, Shuo Wang, *Senior Member, IEEE*, and Qinghai Wang

***Abstract*—Hybrid electromagnetic interference (EMI) filters (HEFs), which are composed of an active filter and a passive filter, have been proposed to reduce the size and weight of conventional passive EMI filters in literatures. However, accurate models that can be used to predict the stability and performance of HEFs have not been developed. To cope with this, this paper presents a modeling technique for a hybrid common-mode (CM) filter. The technique can be applied to the modeling of other HEFs. Critical component models were first developed for the HEF. HEF's overall model was further developed based on these individual component models. Experimental results validated that the developed model can successfully predict the stability and performance of active/hybrid CM filters.**

***Index Terms*—Active EMI filters, CM noise, hybrid EMI filters, modeling, stability analysis.**

I. INTRODUCTION

SWITCHED-MODE power supplies generate conducted electromagnetic interference (EMI) noise due to their fast switching of high currents and high voltages. Various electromagnetic compatibility (EMC) standards [1]–[3] have been applied to both consumer and industry products. Generally, EMI noise includes differential-mode (DM) noise and common-mode (CM) noise. Passive EMI filters, which are composed of inductors and capacitors, are widely used to suppress EMI noise.

As power electronics moves to high power density, EMI filters are becoming one of the biggest function units in the power converters. For CM EMI filters, the maximum CM capacitance is limited by the safety standards so CM inductors usually have a big inductance. Furthermore, the CM inductor windings conduct full power currents so the CM inductors are usually big [2], [4] and heavy [5].

A hybrid filter (HEF) is composed of an active filter and a passive filter. The active filter reduces low-frequency EMI noise and the passive filter reduces high-frequency EMI noise. Because the passive filter has a much higher corner frequency than a conventional EMI filter, the passive filter size is greatly reduced. The total size and weight of the active and passive filters could also be much smaller than a conventional passive EMI filter [4], [6]. At the same time, the HEF could have a better performance than a conventional passive EMI filter because the passive filter has a better high-frequency performance due to its smaller parasitic parameters.

A considerable amount of research has been conducted on HEFs. Various HEFs have been implemented in dc/dc converters, motor drive systems, electric vehicles, etc. [3]–[24]. LaWhite and Schlecht [7] discussed the use of active DM filters in conjunction with minimal passive filters for a high switching frequency converter. Farkas and Schlecht [8] discussed the viability of active EMI filters for utility applications. In [9], a circuit element, nullor, was used to describe the active ripple filters and four basic circuit configurations for ripple current cancellation was classified and compared. Son and Seung-Ki [10] conducted a generalized analysis of active EMI filter topologies. A current-sense current-compensation feedback hybrid EMI filter had been designed for industry application in [11] and [12]. Hybrid EMI filters used in motor drive systems were evaluated and implemented in [4] and [13]–[17]. Recently, a digital active EMI filter was proposed and applied to a microinverter module and a dc/dc converter [18], [19].

The insertion gain and stability for HEFs were discussed in several articles [1], [7], [20]–[22]. Chen *et al.* [20] evaluates the performance of a hybrid CM filter through active impedance multiplication method. In [21], the stability of a current-sense and voltage the feedback active EMI filter was discussed. However, the effect of noise source impedance was missed and experimental validation was not provided. Guidelines on the design of a feed forward voltage-sense voltage-feedback CM HEF was given in [22].

Different from the existing work above, this paper focuses on the development of a modeling technique for a hybrid CM filter. The developed technique can be extended to other HEFs. It would be a good tool for HEF's stability and performance analysis. A hybrid current-sense and current-feedback CM filter is introduced and analyzed in Section II. Critical component models are developed in Section III. The overall model of the hybrid CM filter is further developed based on these individual component models in Section IV. The model is used for stability analysis and is validated by experimental results in Section V. In Section VI, the model is used to evaluate a HEF's performance. It is shown that the developed model can successfully predict the stability and performance of the hybrid CM filter.

Manuscript received July 30, 2015; revised October 10, 2015; accepted November 3, 2015. Date of publication November 20, 2015; date of current version March 25, 2016. This work was supported by Huawei Innovation Research Program. Recommended for publication by Associate Editor A. Lindemann.

Y. Chu is with Texas Instruments, Dallas, TX 75243 USA (e-mail: tmm238@my.utsa.edu).

S. Wang is with the Department of Electrical and Computer Engineering, University of Florida, Gainesville, FL 32611 USA (e-mail: shuowang@ieee.org).

Q. Wang is with Huawei Technologies, Co., Shenzhen 518129 China (e-mail: wangqinghai@huawei.com).

Color versions of one or more of the figures in this paper are available online at http://ieeexplore.ieee.org.

Digital Object Identifier 10.1109/TPEL.2015.2502218

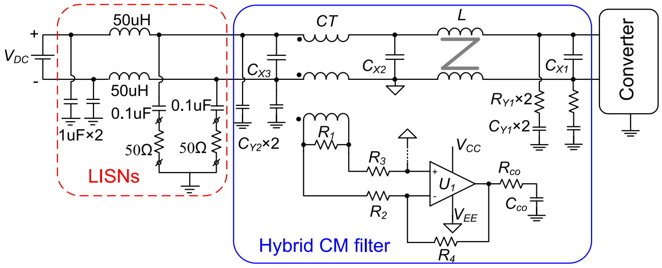

Fig. 1. Hybrid CM filter under investigation.

II. HYBRID CM FILTER UNDER INVESTIGATION

Fig. 1 shows the hybrid CM filter under investigation. In Fig. 1, the CM capacitors $2 \times C_{Y1}$, $2 \times C_{Y2}$, resistors $2 \times R_{Y1}$, and the CM inductor L compose a passive CM filter. The filter reduces the noise ripple and attenuates high-frequency CM noise to ensure the hybrid CM filter works properly [4]. The resistors $2 \times R_{Y1}$ are used to damp resonant peaking of the passive filter. C_{X1}, C_{X2}, and C_{X3} are DM capacitors. A pair of line impedance stabilization networks (LISNs) is connected between a dc source and the hybrid CM filter for conductive EMI measurement.

The active part of the hybrid CM filter is mainly composed of a current transformer (CT), an operational amplifier circuit, and an *RC* branch connected between the output of the operational amplifier and the ground. The CT is a three winding CT used for CM noise current sensing. Its two primary windings are connected to a converter's main power paths. They have the same number of turns and are directly coupled. The CM currents in the main power paths of the converter will generate signals in the third winding on the secondary side. On the other hand, the DM currents will not generate signals in the third winding on the secondary side because the DM magnetic flux is canceled within the CT. R_1 converts the sensed CM currents into voltages. The voltages are fed to an operational amplifier U_1. The noninverting input of U_1 is connected to V_{EE} through an ac capacitor (not shown here). The output of the amplifier is coupled through R_{co} and C_{co} to the ground. This capacitive coupling provides a necessary isolation to meet safety standards. Although the output voltage is fed back to the inverting input via R_4, the operational amplifier injects cancellation currents because its output voltage is the voltage drop of the injected current on the impedance between the output of the operational amplifier and V_{EE}. The dc biasing of the hybrid CM filter is similar to that discussed in [12] and will not be discussed in this paper. Detailed information about this hybrid CM filter can be found in [6], [11], [12], and [20] where similar topologies have been discussed extensively. This paper will concentrate on the modeling and stability analysis of this hybrid CM filter.

III. DEVELOP MODELS FOR CRITICAL COMPONENTS

As discussed in Section II, CT and the operational amplifier are two critical components of the active EMI filter, so their models will be developed in this section.

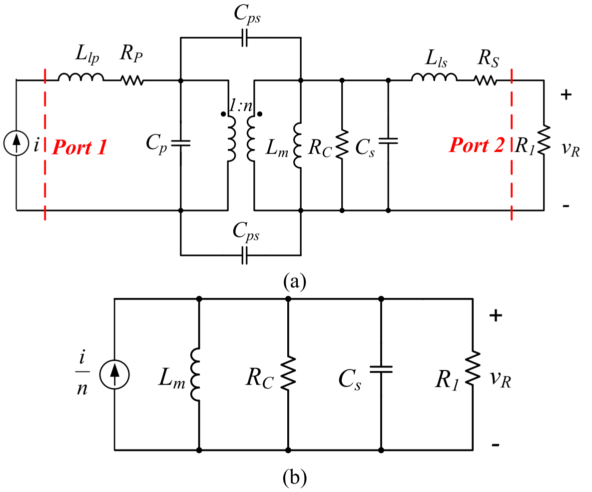

(a)

(b)

Fig. 2. CT model: (a) Model of the CT with parasitic components and (b) simplified CT model.

A. CT Model

As discussed previously, the two primary windings of the CT are in parallel for CM current sensing and the magnetic fluxes generated by the DM currents cancel each other. Thus, the two directly and fully coupled primary windings are equivalent to one winding. Because of this, the CT can be modeled as a two winding CT.

The CT including its parasitics can be modeled as a two-port network as shown in Fig. 2(a) [25]. In Fig. 2(a), C_p and C_s are the lumped intrawinding capacitances within the primary and the secondary windings; L_{lp} and L_{ls} are the leakage inductance of the primary and the secondary windings; R_p and R_s are the resistances of the primary and the secondary windings; two C_{ps} are the interwinding capacitance between the primary and the secondary windings; L_m is the magnetizing inductance on the secondary side; R_C represents the core loss, and CT's turn ratio is 1:n. R_1 is the load resistance at port 2. The current flowing into the primary-side winding is represented by a current source i at port 1 in Fig. 2(a).

The CT's primary winding has only one turn and its turn ratio is 1:7. The CT uses a high permeability ferrite core ($\mu_r = 2300$), which leads to a small leakage inductance (measured as 143 nH) on the secondary side. As a result, the impedance of the leakage inductance is much smaller than the load resistance 100 Ω within the concerned frequency range from 150 kHz to 30 MHz. The CT also has a small (5 mm × 6 mm × 4 mm) size so the winding length is small. As a result, winding resistance and capacitance can be ignored within the concerned frequency range. Because of the analysis above, $C_p, R_p, R_s, L_{lp}, L_{ls}$, and C_{ps} can be ignored in CT's model. Fig. 2(b) shows the simplified CT model after reflecting the primary current to the secondary side. Based on this model, the transimpedance $G_1(s)$ from noise current i to the voltage across the load resistor R_1 can be expressed as

$$G_1(s) = \frac{v_R(s)}{i(s)} = \frac{1}{n} \frac{sL_m R_1 R_c}{s^2 C_s R_1 R_c L_m + sL_m(R_1 + R_c) + R_1 R_c}. \tag{1}$$

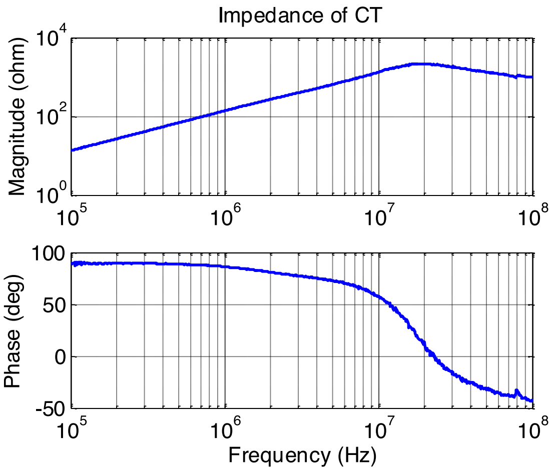

Fig. 3. Measured impedance curves for CT.

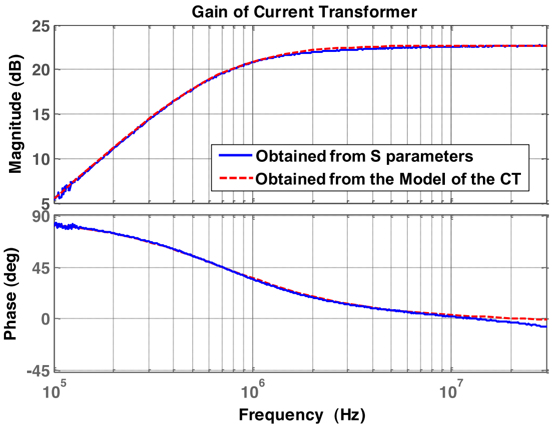

Fig. 4. Comparison of the measured and the predicted transresistance of the CT.

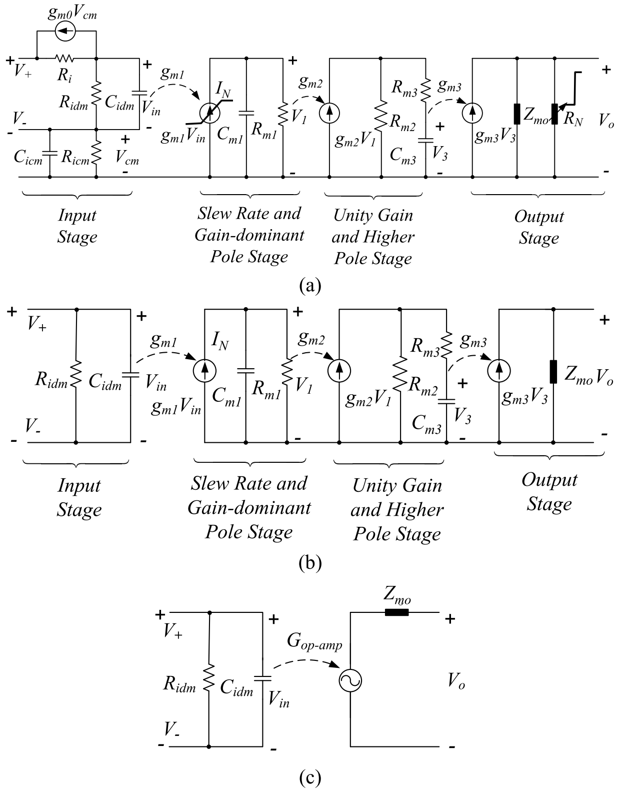

(a)

(b)

(c)

Fig. 5. Operational amplifier model: (a) Four-stage model of the operational amplifier, (b) equivalent circuit of the operational amplifier without the limiters and the CMVR part, and (c) simplified model.

To quantify the parameters of the CT, the impedance of the CT (without the load resistor R_1) was measured from the secondary side when its primary side was open. The measured impedance curves are shown in Fig. 3. Under this configuration, the measured impedance was the impedances of the magnetizing inductance L_m, core loss equivalent resistance R_c, and the parasitic capacitance C_s of the secondary winding in parallel. Based on the measured impedance curve, L_m, R_c and C_s of the CT were calculated as 21.2 μH, 2.043 kΩ, and 2.2 pF, respectively [26]. With these parameters, the transimpedance of the CT $G_1(s)$, from noise current i to the voltage across the load resistor R_1, can be obtained based on (1).

To validate the model of the CT, a 2 × 2 S-parameter matrix $(S_{11}, S_{12}; S_{21}, S_{22})$ was measured between port 1 and port 2 with the load resistor R_1 connected [28], [29]. Based on the measured S-parameters, the transimpedance $G_1(s)$, i.e., the input current to the output voltage gain of the CT was calculated from (2). In (2), Z_{ref} is 50 Ω reference impedance. The gain obtained based on measured S parameters was compared with that obtained according to the CT model, i.e., (1), in Fig. 4. It is shown that the two results match very well. This verifies the developed CT model

$$G_1(s) = \frac{v_R}{i} = Z_{\mathrm{ref}} \frac{2S_{21}}{(1-S_{11})(1-S_{22})-S_{12}S_{21}}. \qquad (2)$$

B. Operational Amplifier Model

In [30], a four-stage operational amplifier model was developed. The four stages include input stage, slew-rate limiting and dominant pole stage, unity gain and higher pole stage, and output stage, as shown in Fig. 5(a). In Fig. 5(a), I_N has a current limiting characteristic. When the current is within the limits, the current source is linear; otherwise, the current will be clamped at either the upper or lower limits. R_N has a voltage limiting characteristic. When the output voltage is within the limits, the resistance is infinite; otherwise, the voltage will be clamped at either upper or lower limits. In Fig. 1, since the CM noise is attenuated by the passive filter to ensure the operational amplifier unsaturated, the nonlinear characteristics of I_N and R_N can be ignored. So R_N can be removed from the model. The effect of the CM voltage on the output voltage of the operational amplifier is also very small due to its high CMRR (80 dB), so the common-mode voltage rejection (CMVR) part, which includes C_{icm}, R_{icm}, and $g_{m0}V_{\mathrm{cm}}$, can also be ignored. R_i is usually much smaller than the impedance of R_{idm} and C_{idm}, so it can be ignored too [30].

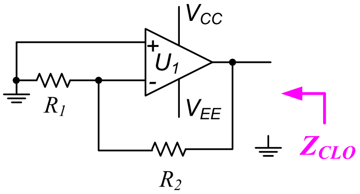

Fig. 6. Close-loop output impedance measurement.

The equivalent circuit of the operational amplifier, therefore, becomes Fig. 5(b).

In the four-stage model in Fig. 5(a), stage 4 is used to model the output impedance and it is connected to stage 3 through the voltage-controlled current source $g_{m3}V_3$. It should not change operational amplifier's Thevenin equivalent output voltage determined by V_3, so g_{m3} should be equal to $1/Z_{mo}$ [30]. The open-loop gain of operational amplifiers can, therefore, be calculated as

$$G_{\text{op-amp}} = \frac{V_o}{V_{\text{in}}} = \frac{g_{m1} g_{m2} R_{m1} R_{m2}}{(1+sC_{m1}R_{m1})\,(1+sC_{m3}(R_{m2}+R_{m3}))} = \frac{G_o}{\left(1+\frac{s}{\omega_1}\right)\left(1+\frac{s}{\omega_2}\right)} \tag{3}$$

where $G_o = g_{m1} g_{m2} R_{m1} R_{m2}$, $\omega_1 = 1/(R_{m1}C_{m1})$, and $\omega_2 = 1/[(R_{m2}+R_{m3})\,C_{m3}]$.

Based on (3), the equivalent circuit of the operational amplifier can be further simplified to Fig. 5(c). In Fig. 5(c), $G_{\text{op-amp}}$ is the open-loop gain of the operational amplifier defined in (3) and R_{idm}, C_{idm}, and Z_{mo} are the input resistance, the input capacitance, and the output impedance of the operational amplifier, which are the same as those in Fig. 5(a) and (b). Based on Fig. 5(c), only $G_{\text{op-amp}}, R_{idm}, C_{idm}$, and Z_{mo} are needed to model the operational amplifier. $G_{\text{op-amp}}$ contains three parameters G_o, ω_1, and ω_2. These parameters can be either found in the datasheet of an operational amplifier or from measurements.

From the datasheet of the operational amplifier used, the input resistance R_{idm} and the input capacitance C_{idm} were found as 10 kΩ and 2.1 pF, respectively. The open-loop gain and phase curves are also given in the datasheet. Based on the gain and phase curves, G_o, ω_1, and ω_2 in (3) were estimated as 5102, 20 kHz, and 250 MHz, respectively.

The open-loop output impedance Z_{mo} was derived from (4) from the close-loop output impedance Z_{CLO} measured with an impedance analyzer. Fig. 6 shows the close loop output impedance measurement setup and Fig. 7 shows the Z_{mo} obtained based on the measurement result. It was found that Z_{mo} can be approximately represented with a 30 Ω resistance based on Fig. 7

$$Z_{mo} = Z_{\text{CLO}} \left[1 + \left(1 + \frac{R_2}{R_1}\right) G_{\text{op-amp}}\right]. \tag{4}$$

Based on these parameters, the model of the operational amplifier was developed.

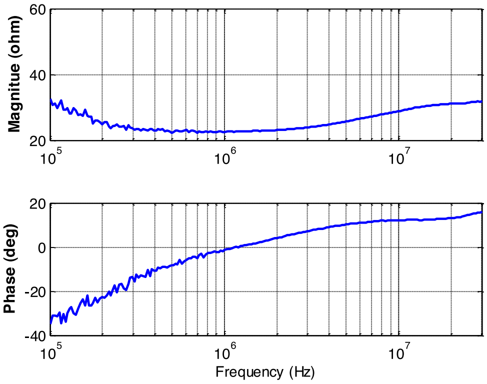

Fig. 7. Calculated open-loop output impedance based on a close-loop measurement.

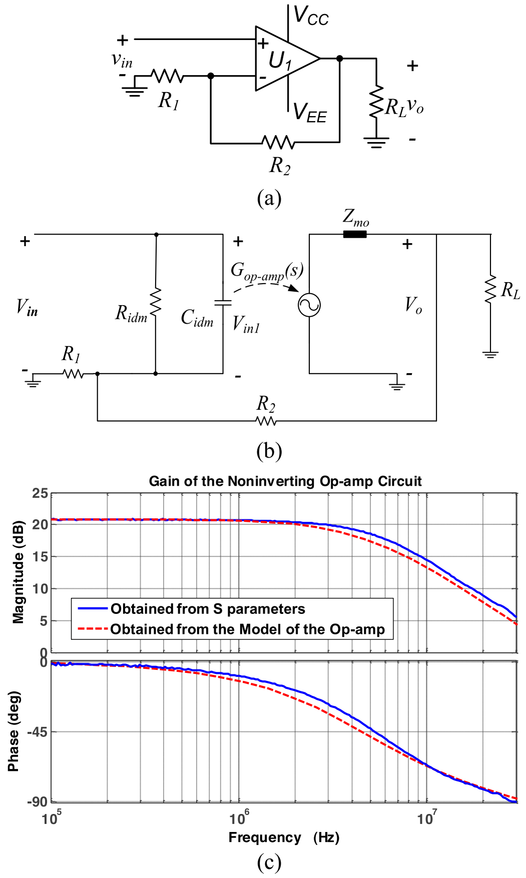

Fig. 8. Validate the developed operational amplifier model: (a) noninverting Op-amp circuit used to validate the developed operational amplifier model, (b) circuit model, and (c) comparison of the measured and the predicted gains.

To validate the developed operational amplifier model, a noninverting configuration shown in Fig. 8(a) was tested in the experiments. R_1, R_2, and R_L are 1 kΩ, 10 kΩ, and 30 Ω, respectively. Fig. 8(b) shows the model for the noninverting configuration. In Fig. 8(b), since the impedance of R_{idm} in parallel with C_{idm} is much larger than R_1, the following two equations hold:

$$V_{\text{in}1} \approx V_{\text{in}} - \frac{R_1 V_o}{R_1 + R_2} \tag{5}$$

$$\frac{G_{\text{op-amp}} V_{\text{in}1} - V_o}{Z_{mo}} \approx \frac{V_o}{R_L} + \frac{V_o}{R_1 + R_2}. \tag{6}$$

According to (5) and (6), the voltage gain of the operational amplifier circuit can be derived as

$$A = \frac{V_0}{V_{\text{in}}} = \frac{\frac{G_{\text{op-amp}}}{Z_{mo}}}{\frac{1}{Z_{mo}} + \frac{1}{R_L} + \frac{1}{R_1+R_2} + \frac{R_1}{R_1+R_2}\frac{G_{\text{op-amp}}}{Z_{mo}}}. \tag{7}$$

The voltage gain is predicted based on the developed model in (7). At the same time, the S-parameter matrix of this network was measured with R_L included and the voltage gain of the operational amplifier circuit was obtained based on the measured S-parameters using [29]

$$G_v = \frac{v_o}{v_{\text{in}}} = \frac{2S_{21}}{(1+S_{11})(1-S_{22}) + S_{21}S_{12}}. \tag{8}$$

The predicted and the measured gains are compared in Fig. 8(c). It is shown that two results match very well except that the model has a pole at 4.5 MHz and the measurement has a pole at 5.1 MHz. The small difference is due to fact that the parameters derived from the datasheet are not exactly the same as an actual IC. However, the difference is within the acceptable range. This validates the developed operational amplifier model.

IV. MODEL DEVELOPMENT FOR THE HYBRID EMI FILTER

To analyze the loop gain, insertion gain and stability of the hybrid EMI filter, the noise source, and the load impedance must be included in the model because they influence the performance of the hybrid EMI filter. In this section, a system model is developed for the hybrid CM filter, which includes the noise source and load impedance, and all the components in the hybrid CM filter used for CM noise attenuation.

The DM capacitors C_{X1}, C_{X2}, and C_{X3} in Fig. 1 are four 4.7 μF ceramic capacitors in parallel and the equivalent series resistance and inductance of each of the 4.7 μF DM capacitors are around 10 mΩ and 0.22 nH. Within the concerned frequency range from 150 kHz to 30 MHz, these capacitors are considered shorted for CM noise since their impedances are very small [27]. Fig. 9(a) shows the equivalent circuit for the CM noise for Fig. 1. The Z_{LISN} is LISNs' CM impedance. It is the load of the hybrid CM filter. For convenience, it can be simply modeled as two 50 Ω resistors in parallel, i.e., a 25 Ω resistor. Under actual conditions, it could be the equivalent impedance of the dc source when LISNs are not present. V_s and Z_s are the CM noise source and its impedance which are determined by the power converter; Z_{c1} represents the impedance of the two paralleled branches that are composed of the damping resistors $2 \times R_{Y1}$, and the CM capacitors $2 \times C_{Y1}$; Z_{c2} represents the two paralleled CM capacitors $2 \times C_{Y2}$; Z_{co} is the impedance of the injecting *RC* branch which is composed of R_{co} and C_{co}; Z_{CT} is the impedance of the CT, and Z_{out} is the close-loop output impedance of the operational amplifier circuit. *G*(*s*) in Fig. 9(a) is the gain from the CM noise current to the output voltage of the active filter. It includes the effects of CT and the operational amplifier circuit, as shown in Fig. 9(b). In Fig. 9 (b), the input impedance Z_{in} of the operational amplifier circuit is given by [31]

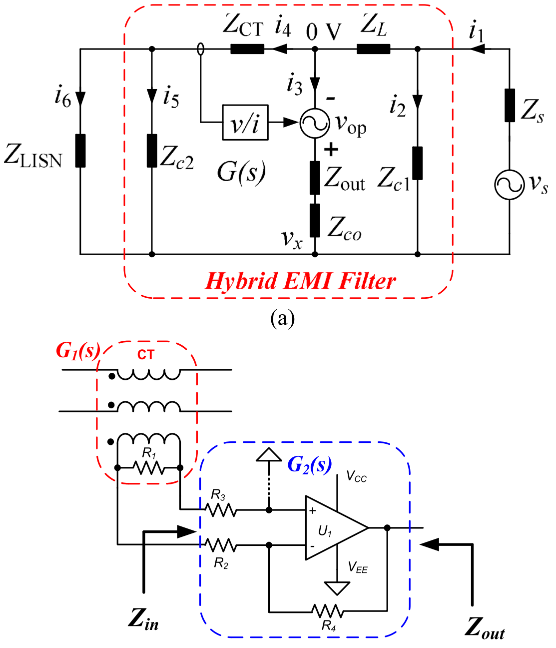

(a)

(b)

Fig. 9. (a) Equivalent circuit of the system with the hybrid CM filter and (b) circuit of *G*(*s*) in Fig. 9(a).

$$Z_{\text{in}} = R_2 + R_3 + \frac{Z_{idm}}{1 + [1 + G_{\text{op-amp}}(s)]\,\frac{Z_{idm}}{R_4}} \tag{9}$$

where Z_{idm} is the impedance of R_{idm} and C_{idm} in parallel.

In this case, Z_{in} is much larger than R_1, so $Z_{\text{in}}'s$ loading effects can be ignored. $G_1(s)$ and $G_2(s)$ can be decoupled. As a result, *G*(*s*) equals to $G_1(s)G_2(s)$, where $G_1(s)$ and $G_2(s)$ are the gains of the CT and the operational amplifier circuit, respectively.

In Fig. 9(a), i_3 is the output current of the active filter. i_4 is the CM noise current sensed by the CT. Other currents in each branch are shown in Fig. 9(a).

As shown in Fig. 9(a), the output voltage v_{op} of the active filter is

$$v_{\text{op}} = i_4 G(s). \tag{10}$$

If the dc bus is defined as CM voltage reference, i.e., 0 V, based on Kirchhoff's current law and Kirchhoff's voltage law, equations (11)–(17) hold

$$v_s = i_1 Z_s + i_2 Z_{c1} \tag{11}$$

$$i_1 = i_2 + i_3 + i_4 \tag{12}$$

$$i_3 = \frac{v_{\text{op}} - v_x}{Z_{\text{out}} + Z_{co}} \tag{13}$$

$$i_2 = \frac{(i_3 + i_4)\,Z_L - v_x}{Z_{c1}} \tag{14}$$

$$i_4 = \frac{-v_x}{Z_{\text{CT}} + Z_{\text{LISN}}//Z_{c2}} \tag{15}$$

$$i_4 = i_5 + i_6 \tag{16}$$

$$i_6 Z_{\text{LISN}} = i_5 Z_{c2}. \tag{17}$$

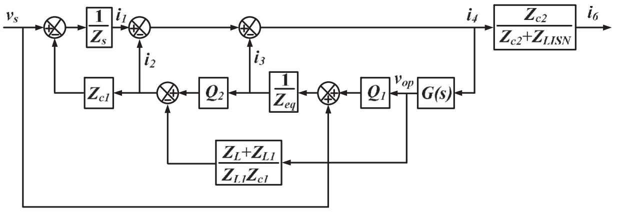

Fig. 10. Block diagram of the system.

From equations above, the following equations can be derived

$$i_3 = \frac{v_s + Q_1 v_{\text{op}}}{Z_{\text{eq}}} \tag{18}$$

$$i_2 = i_3 Q_2 - v_{\text{op}} \frac{Z_L + Z_{L1}}{Z_{L1} Z_{c1}} \tag{19}$$

where

$$\begin{aligned} Q_1 &= \frac{Z_s}{Z_{L1}} + (Z_s + Z_{c1}) \frac{Z_L + Z_{L1}}{Z_{L1} Z_{c1}}, \\ Q_2 &= \frac{Z_L}{Z_{c1}} + \frac{(Z_{co} + Z_{\text{out}})}{Z_{L1}} \frac{(Z_L + Z_{L1})}{Z_{c1}}, \\ Z_{\text{eq}} &= Z_s + \frac{Z_s (Z_{co} + Z_{\text{out}})}{Z_{L1}} + (Z_s + Z_{c1}) \\ &\quad \times \left(\frac{Z_L}{Z_{c1}} + \frac{(Z_L + Z_{L1})}{Z_{c1}} \frac{(Z_{co} + Z_{\text{out}})}{Z_{L1}} \right), \end{aligned}$$

and

$$Z_{L1} = Z_{\text{CT}} + Z_{\text{LISN}} // Z_{c2}.$$

Based on the above equations, the signal flow block diagram of the system can be derived in Fig. 10. According to the block diagram, the loop gain of the system can be derived as (20), which can be used to evaluate the stability of the system. According to Mason's rule, the transfer function from v_s to i_6 can be obtained as

$$G_{\text{loop}} = \frac{G(s)}{Z_{\text{eq}}} \left(\frac{Z_s}{Z_{L1}} + \frac{Z_L}{Z_{c1} Z_{L1}} (Z_s + Z_{c1}) \right) \tag{20}$$

$$\frac{i_6}{v_s} = \frac{\left(\frac{(Z_{co} + Z_{\text{out}})}{Z_{\text{eq}} Z_{L1}} \right) \left(\frac{Z_{c2}}{Z_{c2} + Z_{\text{LISN}}} \right)}{1 + \frac{G(s)}{Z_{\text{eq}}} \left(\frac{Z_s}{Z_{L1}} + \frac{Z_L}{Z_{c1} Z_{L1}} (Z_s + Z_{c1}) \right)}. \tag{21}$$

The noise current flowing through the LISNs without the hybrid CM filter is given by (22). The insertion gain of the hybrid CM filter can be calculated based on (23)

$$i_6' = \frac{v_s}{Z_{\text{LISN}} + Z_s} \tag{22}$$

$$G_{\text{insertion}} = \frac{i_6}{i_6'}. \tag{23}$$

Based on the previous analysis, the performance and stability of the hybrid CM filter can be evaluated with the developed model. This is very critical for the design and industrial application of a hybrid CM filter. To design a hybrid CM filter, an operational amplifier needs to be selected. First, the operational amplifier should have enough output capability to inject enough cancellation currents. Second, it should not get saturated at the highest output voltages. With a high operation power supply voltage, the operational amplifier will not easily get saturated, but it leads to a relatively high power loss. On the other hand, with a low operation power supply voltage, the operational amplifier may be easy to get saturated, but it leads to a relatively low power loss. For the hybrid CM filters used in dc/dc converters, the power loss of the operational amplifier is usually small, so high operation voltage is generally preferred if possible. Third, the operational amplifier should have enough unity-gain bandwidth to ensure that it can successfully amplify the noise voltage within a wide bandwidth. After the operational amplifier is decided, the passive components including CT, capacitors, inductors, and damping resistors can be designed to ensure the stability and performance of the hybrid CM filter based on the developed model.

TABLE I
KEY PARAMETERS OF THE UNSTABLE AND STABLE SCENARIOS UNDER INVESTIGATION

	Unstable Scenario	Stable Scenario
Damping resistor, R_{Y1}	0 Ω	2 Ω
CM capacitor at noise source side, C_{Y1}	11 nF	11 nF
CM inductor, L	No	No
CM capacitor at LISN side, C_{Y2}	No	No
Load resistor of the CT, R_1	100 Ω	100 Ω
Resistors at the input of the Op-amp, R_2, R_3	100 Ω	100 Ω
Feedback resistor of Op-amp, R_4	51 kΩ	51 kΩ
Injection resistor, R_{co}	4.7 Ω	4.7 Ω
Injection capacitor, C_{co}	100 nF	100 nF

V. STABILITY ANALYSIS

The stability of the system was investigated in two scenarios with the model developed. The two scenarios consist of a stable scenario and an unstable scenario. The key parameters of the hybrid CM filter used in the analysis are summarized in Table I. The circuits of the two scenarios were almost the same except there was no R_{Y1} in the unstable scenario and R_{Y1} was 2 Ω in the stable scenario. These two scenarios were used to validate the stability analysis. The final actual scenarios could be different, but the technique developed still holds.

In the stable scenario, the power converter was powered off and the hybrid CM filter was powered on. A spectrum analyzer measured no EMI noise on the LISNs. In the unstable scenario, the power converter was still powered off and the hybrid CM filter was still powered on. The spectrum analyzer measured a high noise spike spectrum. Fig. 11 shows the comparison.

The first spike around 3.3 MHz was due to the resonance under unstable scenario and the other spikes were the harmonics. Fig. 12 shows the measured voltage drop of the output current on R_{co} (4.7 Ω) in the two scenarios.

In Fig. 12, for unstable scenario, the measured voltage is a trapezoidal wave with a fundamental frequency around

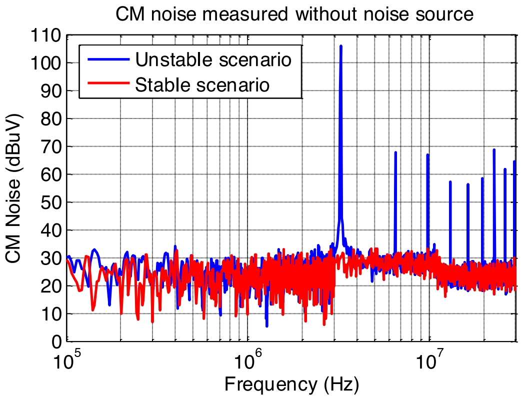

Fig. 11. CM noise comparison between unstable and stable operations.

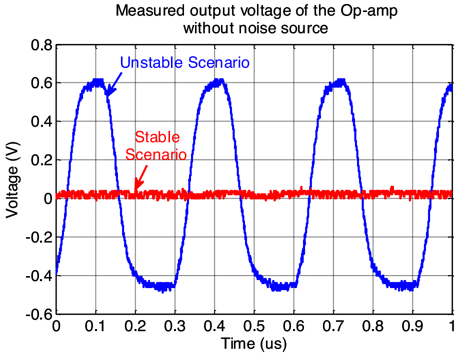

Fig. 12. Time-domain measurement results of the output voltages of the operational amplifier without noise source in the two scenarios.

3.3 MHz, while for stable scenario, it was zero. The results match the spectrum measurement results in Fig. 11.

The output impedance Z_{out} of the operational amplifier circuit is in Fig. 9(b) is [31]

$$Z_{\text{out}} = \frac{Z_{mo}}{1 + \frac{Z_{mo} + G_{\text{op-amp}}(s)(R_2 + R_3)}{R_2 + R_3 + R_4}}. \tag{24}$$

At 3.3 MHz, the operational amplifier's open-loop gain $G_{\text{op-amp}}$ is low. Since $R_4 \gg R_2 + R_3$, it was found that $Z_{\text{out}} \approx Z_{mo}$.

Although the peak-to-peak voltage of the trapezoidal wave was only around 1.1 V in Fig. 12, when Z_{out} and other impedances in the circuit are taken into consideration, the actual output voltage of the operational amplifier in the unstable scenario is around 8.5 V, which is very close to 9 V, the power supply voltage of the operational amplifier. So in the unstable scenario, due to the saturation of the operational amplifier, the output resonant voltage of the operational amplifier became the trapezoidal wave in Fig. 12. This was why there are harmonics of 3.3 MHz.

Based on (9), the calculated input impedance Z_{in} of the operational amplifier circuit is much higher than CT's load resistance R_1. The loop gain can, therefore, be measured as in Fig. 13. In the measurement, the noise source v_s was shorted. In Fig. 13, v_1 is voltage excitation, v_2 is the response, and v_2/v_1 is the loop gain.

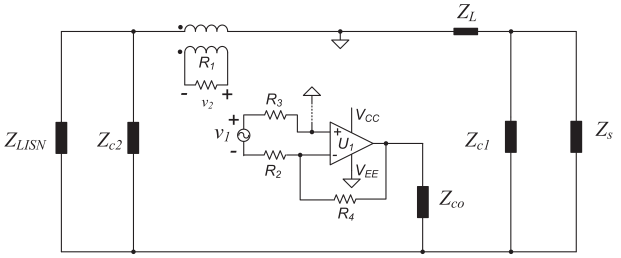

Fig. 13. Loop gain measurement.

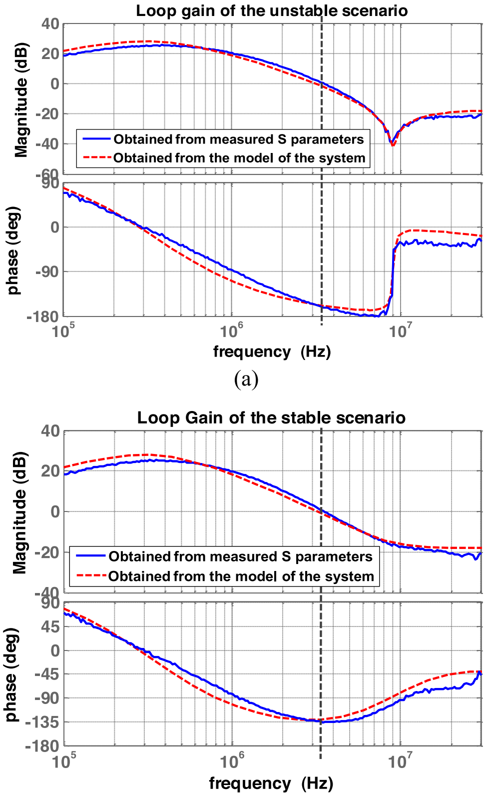

(a)

(b)

Fig. 14. Comparison of the measured and calculated loop gains: (a) unstable scenario and (b) stable scenario.

The loop gains v_2/v_1 for both scenarios were measured using S-parameters and transformed to voltage gain [29]. The loop gains are also calculated based on (20). In the calculation, the impedance Z_{c1} includes 22 nF capacitance, 0.023 Ω ESR, and 7.1 nH ESL. On Z_{co} and Z_{LISN} branches, there were resistors, so effects of the high-frequency parasitics on these two branches were ignored in the calculation. Source impedance Z_s, which is the impedance of parasitic capacitance, is much higher than Z_{c1}, so $Z_s//Z_{c1} \approx Z_{c1}$.

Fig. 14(a) and (b) shows the comparison between the measured and the calculated loop gains for both scenarios. They match very well for both scenarios. In addition, in Fig. 14(a), it is shown the crossover frequency of the unstable case is 3.3 MHz and at that frequency, the phase margin is only 15°. It is not enough to ensure a stable system. This agrees with the measurement results in Figs. 11 and 12. For the stable scenario,

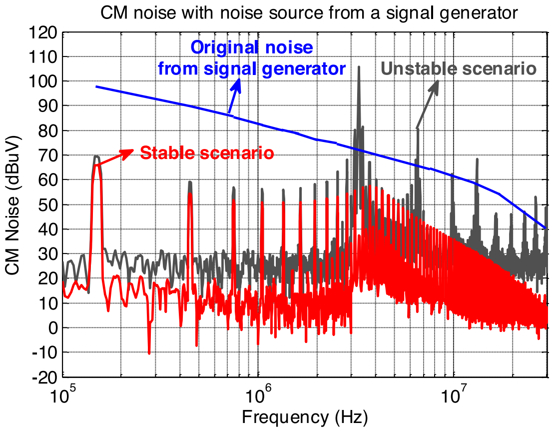

Fig. 15. CM noise measured with a 500-mV 100-kHz square wave from a signal generator noise source.

the phase margin was increased to 45° due to the presence of R_{Y1}.

To further validate the stability analysis, a signal generator with 50 Ω source impedance was used as a noise source. A 500-mV 150-kHz square wave was fed to the hybrid CM filter. The measurement results are shown in Fig. 15. Based on Fig. 13, Z_{c1} branch is in parallel with the noise source impedance in the loop gain calculation. In this case, the noise source impedance is 50 Ω, which is much larger than that of Z_{c1} branch, so $Z_s//Z_{c1} \approx Z_{c1}$. As a result, the loop gain of the two scenarios with the signal generator are the same as Fig. 14. Fig. 15 agrees with the prediction in Fig. 14. Instability occurred at 3.3 MHz if R_{Y1} is not connected.

Finally, a dc/dc converter was used as the noise source for the hybrid CM filters, as shown in Fig. 16(a). It should be pointed out that in Table I, the L in Fig. 1 was removed, so the CM noise added to the active CM filter has high *di*/*dt* and high amplitude. To ensure that the active CM filters work properly [4] with the power converter, a 200-μH CM inductor was added between the dc/dc converter and Z_{c1} to reduce *di/dt* and noise amplitude, as shown Fig. 16(a). Based on [32], the noise source impedance of the dc/dc converter was estimated as a 7 nF capacitance, a 15 Ω resistance, and a 0.6 μH inductance in series. The impedance of the inductor was an equivalent part of the noise source impedance. Due to the small impedance of Z_{c1}, the impedance of $Z_{c1}//Z_s$ is still determined by Z_{c1}. As a result, the loop gains of the two scenarios with the converter are still the same as Fig. 14. The measurement results shown in Fig. 16(b) validate the above analysis. Instability occurred at 3.3 MHz if R_{Y1} is not connected.

VI. PERFORMANCE EVALUATION FOR THE HYBRID CM FILTER WITH THE DEVELOPED MODEL

The insertion gain of a hybrid CM filter was investigated with the developed model for an actual setup same as Fig. 1. The key parameters of the hybrid CM filter are summarized in Table II.

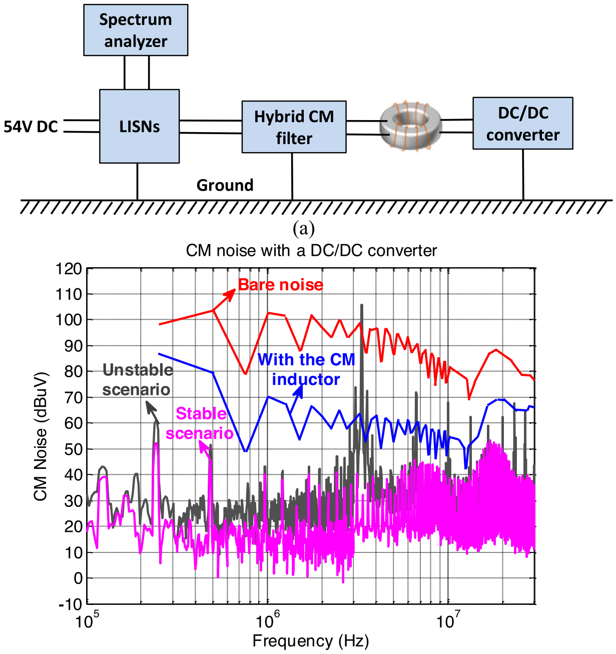

(a)

(b)

Fig. 16. Measured CM noise with a dc/dc power converter: (a) Measurement setup and (b) measured CM noise in the two scenarios.

TABLE II
KEY PARAMETERS OF THE HYBRID CM FILTER UNDER INVESTIGATION

Damping resistor, R_{Y1}	2 Ω
CM capacitor at noise source side, C_{Y1}	11 nF
CM inductor, L	0.5 μH
CM capacitor at LISN side, C_{Y2}	44 nF
Load resistor of the CT, R_1	100 Ω
Resistors at the input of the Op-amp, R_2 , R_3	100 Ω
Feedback resistor of Op-amp, R_4	150 kΩ
Injection resistor, R_{co}	33 Ω
Injection capacitor, C_{co}	100 nF

The system's stability was first analyzed based on the developed model. It was found that the system was stable with 85° phase margin. The S-parameters of the hybrid CM filter were then measured. Based on the measured S-parameters, the insertion gain of the hybrid CM filter was calculated according to Wang *et al.* [28]. The insertion gain of the hybrid CM filter was also predicted based on the model developed previously. In the prediction, the noise source impedance, the parasitic resistances, and inductances of Z_{c1} branch and Z_{c2} branch were all taken into consideration. The same source impedance of the dc/dc converter used in Fig. 16(a) was used. The parasitic resistance and inductance of Z_{c2} branch were 0.05 Ω and 8.1 nH, respectively. The very small parasitics of the 0.5 μH CM inductor were ignored. Fig. 17 shows the comparison of the insertion gain calculated from the measured S-parameters with that predicted based on the model. Two results match very well. It validates that the developed model can successfully predict the insertion gain of the hybrid CM filter.

The CM EMI was also tested with the dc/dc converter. The measurement results and the predicted CM noise with the hybrid CM filter are shown in Fig. 18. In Fig. 18, it is shown that the predicted CM noise with the hybrid CM filter can match the

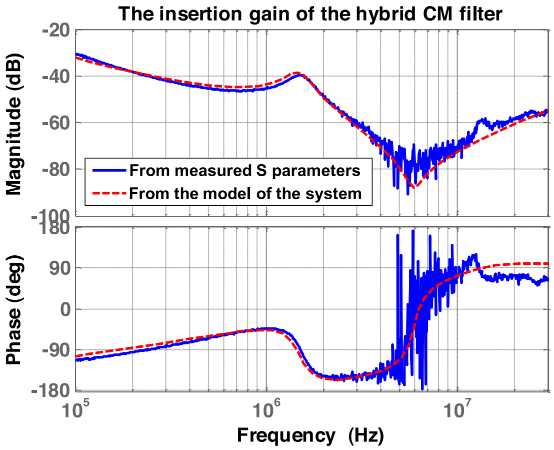

Fig. 17. Comparison of the predicted and measured insertion gains of the hybrid CM filter.

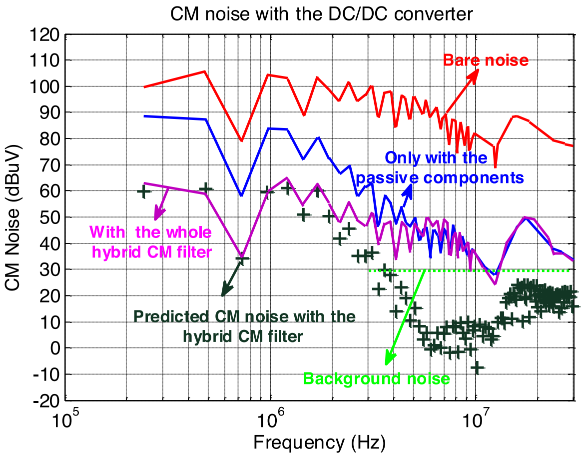

Fig. 18. Measured and predicted CM noise.

measurement results up to 2 MHz. The high-frequency mismatch of the two results was due to other factors such as the background noise, grounding and near-field coupling [26], [33]–[35], etc. However, the high-frequency noise was mainly attenuated with the passive part of the hybrid CM filter. So, the developed model is very helpful in the evalution and design of the active part.

VII. CONCLUSION

In this paper, the model of a hybrid CM filter is developed. The models for CT and the operational amplifier are first developed. The model of the hybrid CM filter including the noise source and the load is further developed. With the developed model, the stability of the system and the performance of the hybrid CM filter were effectively evaluated. The developed models were verified through experiments. The experimental results show that the developed model can successfully predict the stability and low-frequency performance of the hybrid CM filter. This would greatly benefit the design and application of the hybrid CM filters in power electronics systems. The procedure developed in this paper can be used to model other types of HEFs.

REFERENCES

[1] K. Mainali and R. Oruganti, "Conducted EMI Mitigation techniques for switch-mode power converters: A survey," *IEEE Trans. Power Electron.*, vol. 25, no. 9, pp. 2344–2356, Sep. 2010.

[2] R. P. Clayton, *Introduction to Electromagnetic Compatibility*, 2nd ed. Hoboken, NJ, USA: Wiley, 2006.

[3] M. Ali, E. Laboure, and F Costa, "Integrated active filter for differential-mode noise suppression," *IEEE Trans. Power Electron.*, vol. 29, no. 3, pp. 1053–1057, Mar. 2014.

[4] S. Wang, Y. Y. Maillet, F. Wang, D. Boroyevich, and R. Burgos, "Investigation of hybrid EMI filters for common-mode EMI suppression in a motor drive system," *IEEE Trans. Power Electron.*, vol. 25, no. 4, pp. 1034–1045, Apr. 2010.

[5] W. Chen, W. Zhang, X. Yang, Z. Sheng, and Z. Wang, "An experimental study of common- and differential-mode Active EMI filter compensation characteristics," *IEEE Trans. Electromagn. Compat.*, vol. 51, no. 3, pp. 683–691, Aug. 2009.

[6] W. Chen, X. Yang, and Z. Wang, "An active EMI filtering technique for improving passive filter low-frequency performance," *IEEE Trans. Electromagn. Compat.*, vol. 48, no. 1, pp. 172–177, Feb. 2006.

[7] L. LaWhite and M. F. Schlecht, "Design of active ripple filters for power circuits operating in the 1–10 MHz range," *IEEE Trans. Power Electron.*, vol. 3, no. 3, pp. 310–317, Jul. 1988.

[8] T. Farkas and M. F. Schlecht, "Viability of active EMI filters for utility applications," *IEEE Trans. Power Electron.*, vol. 9, no. 3, pp. 328–337, May 1994.

[9] N. K. Poon, J. C. P. Liu, C. K. Tse, and M. H. Pong, "Techniques for input ripple current cancellation: classification and implementati-on," *IEEE Trans. Power Electron.*, vol. 15, no. 6, pp. 1144–1152, Nov. 2000.

[10] Y.-C. Son and S. Seung-Ki, "Generalization of active filters for EMI reduction and harmonics compensation," *IEEE Trans. Ind. Appl.*, vol. 42, no. 2, pp. 545–551, Mar./Apr. 2006.

[11] J. Dumas, B. Lanoue, and B. Tahhan, "Active analog power filters provide solutions for EMC and EMI," in *Proc. IEEE Appl. Power Electron. Conf.*, 2004, pp. 675–680.

[12] M. Briere, J. Dumas, and B. Tahhan, "EMI filter circuit," U.S. Patent 6 898 092 B2, May 24, 2005.

[13] M. C. Di Piazza, A. Ragusa, and G. Vitale, "An optimized feedback common mode active filter for vehicular induction motor drives," *IEEE Trans. Power Electron.*, vol. 26, no. 11, pp. 3153–3162, Nov. 2011.

[14] W. Chen, X. Yang, J. Xue, and F. Wang, "A novel filter topology with active motor CM impedance regulator in PWM ASD system," *IEEE Trans. Ind. Electron.*, vol. 61, no. 12, pp. 6938–6946, Dec. 2014.

[15] P. Pairodamonchai, S. Suwankawin, and S. Sangwongwanich, "Design and implementation of a hybrid output EMI filter for high-frequency common-mode voltage compensation in PWM inverters," *IEEE Trans. Ind. Appl.*, vol. 45, no. 5, pp. 1647–1659, Sep./Oct. 2009.

[16] M. C. Di Piazza, M. Luna, and G. Vitale, "EMI reduction in DC-fed electric drives by active common-mode compensator," *IEEE Trans. Electromagn. Compat.*, vol. 56, no. 5, pp. 1067–1076, Oct. 2014.

[17] C. Zhu and T. H. Hubing, "An active cancellation circuit for reducing electrical noise from three-phase AC motor drivers," *IEEE Trans. Electromagn. Compat.*, vol. 56, no. 1, pp. 60–66, Feb. 2014.

[18] D. Hamza, Q. Mei, and P. K. Jain, "Application and stability analysis of a novel digital active EMI filter used in a grid-tied PV microinverter module," *IEEE Trans. Power Electron.*, vol. 28, no. 6, pp. 2867–2874, Jun. 2013.

[19] D. Hamza, M. Pahlevaninezhad, and P. K. Jain, "Implementation of a novel digital active EMI technique in a DSP-based DC–DC digital controller used in electric vehicle (EV)," *IEEE Trans. Power Electron.*, vol. 28, no. 7, pp. 3126–3137, Jul. 2013.

[20] W. Chen, X. Yang, and Z. Wang, "A novel hybrid common-mode EMI filter with active impedance multiplication," *IEEE Trans. Ind. Electron.*, vol. 58, no. 5, pp. 1826–1834, May 2011.

[21] K. Mainali and R. Oruganti, "Design of a current-sense voltage-feedback common mode EMI filter for an off-line power converter," in *Proc. IEEE Power Electron. Spec. Conf.*, 2008, pp. 1632–1638.

[22] D. Shin, S. Kim, G. Jeong, J. Park, J, Park, K. J. Han, and J. Kim, "Analysis and design guide of active EMI filter in a compact package for reduction of common-mode conducted emissions," *IEEE Trans. Electromagn. Compat.*, vol. 57, no. 4, pp. 660–671, Aug. 2015.

[23] X. Chang, W. Chen, Y. Yang, K. Wang, and X. Yang, "Research and realization of a novel active common-mode EMI filter," in *Proc. IEEE Appl. Power Electron. Conf.*, 2015, pp. 1941–1945.

[24] D. Hamza, M. Sawan, and P. K. Jain, "Suppression of common-mode input electromagnetic interference noise in DC-DC converters using the active filtering method," *IET Trans. Power Electron.*, vol. 4, no. 7, pp. 776–784, Aug. 2011.

[25] N. Kondrath and M. K. Kazimierczuk, "Bandwidth of current transformers," *IEEE Trans. Instrum. Meas.*, vol. 58, no. 6, pp. 2008–2016, Jun. 2009.

[26] Y. Chu, S. Wang, N. Zhang, and D. Fu, "A common mode inductor with external magnetic field immunity, low magnetic field emission and high differential mode inductance," *IEEE Trans. Power Electron.*, vol. 30, no. 12, pp. 6684–6694, Dec. 2015.

[27] Y. Chu and S. Wang, "A generalized common-mode current cancelation approach for power converters," *IEEE Trans. Ind. Electron.*, vol. 62, no. 7, pp. 4130–4140, Jul. 2015.

[28] S. Wang, F. C. Lee, and W. G. Odendaal, "Characterization and parasitic extraction of EMI filters using scattering parameters," *IEEE Trans. Power Electron.*, vol. 20, no. 2, pp. 502–510, Mar. 2005.

[29] S. Wang, F. C. Lee, and W. G. Odendaal, "Using scattering parameters to characterize EMI filters," in *Proc. IEEE Power Electron. Spec. Conf.*, 2004, pp. 297–303.

[30] E. Sanchez-Sinencio and M. L. Majewski, "A nonlinear macromodel of operational amplifiers in the frequency domain," *IEEE Trans. Circuits Syst.*, vol. CAS-26, no. 6, pp. 395–402, Jun. 1979.

[31] P. R. Gray, P. J. Hurst, S. H. Lewis, and R. G. Meyer, *Analysis and Design of Analog Intergrated Circuits*. New York, NY, USA: Wiley, 2009

[32] D. Zhang, D. Y. Chen, M. J. Nave, and D. Sable, "Measurement of noise source impedance of off-line converters," *IEEE Trans. Power Electron.*, vol. 15, no. 5, pp. 820–825, Sep. 2000.

[33] Y. Chu, S. Wang, J. Xu, and D. Fu, "EMI reduction with near field coupling suppression techniques for planar transformers and CM chokes in switching-mode power converters," in *Proc. IEEE Energy Convers. Congr. Expo.*, 2013, pp. 3679–3686.

[34] S. Wang, Y. Y Maillet, F. Wang, R. Lai, F. Luo, and D. Boroyevich, "Parasitic effects of grounding paths on common-mode EMI filter's performance in power electronics systems," *IEEE Trans. Ind. Electron.*, vol. 57, no. 9, pp. 3050–3059, Sep. 2010.

[35] S. Wang, J. D. Van Wyk, and F. C. Lee, "Effects of interactions between filter parasitics and power interconnects on EMI filter performance," *IEEE Trans. Ind. Electron.*, vol. 54, no. 6, pp. 3344–3352, Dec. 2007.

Yongbin Chu (S'12) received the B.S.E.E. degree from the Hefei University of Technology, Hefei, China, in 2011, and the Ph.D. degree from the University of Texas at San Antonio, San Antonio, TX, USA, in 2015.

His interest includes circuit topology for power electronics, EMI/EMC in power electronics systems, high-efficiency and high power density power conversion, and power systems analysis. He has published more than ten IEEE journal and conference papers.

Shuo Wang (S'03–M'06–SM'07) received the Ph.D. degree from Virginia Tech, Blacksburg, VA, USA, in 2005.

He has been an Associate Professor at the Department of Electrical and Computer Engineering, University of Florida, Gainesville, FL, USA, since 2015. From 2010 to 2014, he was with the University of Texas at San Antonio, San Antonio, TX, USA, first as an Assistant Professor and later as an Associate Professor. From 2009 to 2010, he was a Senior Design Engineer with GE Aviation Systems, Vandalia, OH, USA. From 2005 to 2009, he was a Research Assistant Professor with Virginia Tech. He has published more than 110 IEEE journal and conference papers and holds seven U.S. patents.

Dr. Wang received the Best Transaction Paper Award from the IEEE Power Electronics Society in 2006 and two William M. Portnoy Awards for the papers published in the IEEE Industry Applications Society in 2004 and 2012, respectively. In 2012, he received the prestigious National Science Foundation CAREER Award. He is an Associate Editor for the IEEE TRANSACTIONS ON INDUSTRY APPLICATIONS and a Technical Program Cochair for the IEEE 2014 International Electric Vehicle Conference.

Qinghai Wang received the B.Eng. degree in electrical engineering from Xi'an Jiaotong University, Xi'an, China, in 2001.

After graduation, he was with Huawei Technologies, Co., Ltd., Shenzhen, China, where he was involved in EMC and Surge protection design and research for ICT& Power module. He is currently a Chief Design Engineer and the Leader of EMC and Lightning Technology Manage Group. He had made outstanding contributions to protection circuit design, the miniaturization of protection and filter circuits, LF filter design and grounding design, etc. His current research interest includes EMI modeling and system simulation, EMI suppression, and passive and active filter design for power electronic product. He is a Member of several standard organizations and has been responsible for the constituting of several standards, and holds 12 patents.